PAPER

Sputtered Si and Mg doped hydroxyapatite for biomedical applications

View the article online for updates and enhancements.

IOP ebooks™

Bringing you innovative digital publishing with leading voices to create your essential collection of books in STEM research.

Start exploring the collection - download the first chapter of every title for free.

Biomedical Materials

CrossMark

PAPER

Sputtered Si and Mg doped hydroxyapatite for biomedical applications

Alina Vladescu[1,7], Cosmin Mihai Cotrut[2,7] , Funda Ak Azem[3], Mirosław Bramowicz[4], Iulian Pana[1,5], Viorel Braic[1], Isil Birlik[3], Adrian Kiss[1], Mariana Braic[1], Radwan Abdulgader[6], Robin Booysen[6], Sławomir Kulesza[4] and Thomas K Monsees[6]

1   National Institute for Optoelectronics, 409 Atomistilor St., Magurele, Romania
2   University Politehnica of Bucharest, 313 Spl. Independentei, Bucharest, Romania
3   Dokuz Eylul University, Engineering Faculty, Metallurgical and Materials Engineering Department, Tinaztepe Campus, Izmir, Turkey
4   Warmia and Mazury University in Olsztyn, Oczapowskiego 2, Olsztyn, 10-719, Poland
5   Faculty of Physics, University of Bucharest, 405 Atomistilor St., Magurele, Romania
6   Department of Medical Biosciences, University of the Western Cape, Bellville, South Africa
7   National Research Tomsk Polytechnic University, Lenin Avenue 43, Tomsk, 634050, Russia

E-mail: cosmin.cotrut@upb.ro

Abstract

Hydroxyapatite (HAP) coatings are applied on metallic implant materials to combine mechanical properties of metallic material with bioactivity abilities of HAP ceramic. In this study, HAP coatings with additions of Si and Mg are proposed to be deposited on Ti6Al4V substrates by RF magnetron sputtering. Chemical bonding, morphology, topography and corrosion resistance in simulated body fluids (SBF) of the coatings were investigated. Additionally, mechanical and biological properties of the coatings were evaluated. It was found that the addition of Si and Mg does not influence the formation of a HAP phase. All the coatings exhibited smooth surface and uniform growth, without defects or cracks. Both hardness and elastic modulus of the coated samples decrease with Mg addition in the HAP-Si structure. Both Mg and Si addition into HAP coatings were found to enhance the corrosion resistance of the Ti6Al4V alloy in the SBF solution. Coatings with low Mg content exhibited better corrosion performance. All the coatings investigated were biocompatible, as demonstrated by SaOS-2 bone cell attachment and growth. However, cell proliferation and morphology were inferior on samples with the highest Mg content.

1. Introduction

For dental and orthopaedic implants to succeed, it is important to ensure a good bond between the implants and bone [1–3]. Biomaterials with high wear and corrosion resistance during the exposure of implants to human tissues and fluids [4–7], and suitable mechanical properties for minimizing the stress-shielding effect [8–11], are required for such orthopaedic applications. The main drawback of orthopaedic implants is the weak fixation between the implant and human bone [12–15]. Up to now, cemented prostheses have been used to fix it to the bone. Unfortunately, these have some major drawbacks, which limit their usage in orthopaedic applications, such as: (i) the cement can undergo fatigue fracture, and this leads to loosening of the implant;

(ii) the cement particles and wear debris can activate the immune system, leading to bone resorption; (iii) the cement monomer is absorbed by the blood and ends up in the heart, which may cause intraoperative deaths. The first two effects may lead to rejection of the artificial joint, in which case revision surgery is necessary [12–15]. For the third reason, many surgeons prefer cementless prostheses. However, even these prostheses exhibit some disadvantages. Firstly, cementless prostheses should be placed in healthy bones [16]. Secondly, more than three months are needed for bone to grow on an implant surface [16]. Besides this, cementless hip or knee implants are textured, and during fixation there are some friction processes between the implant and the bone [7, 17]. As all of these processes can lead to a loosening of the orthopaedic implants, revision surgery might be

necessary. This would imply a new trauma for the patient. Thus, in recent years, research has focused on improving the strength of the implant-tissue interface. One way is to coat the implant surface, to develop implants with high biocompatibility and bioactivity capabilities. Hence, to improve bone ingrowth of uncemented prostheses, the application of calcium phosphate (CaP) as coatings was performed [18]. Thus, the main goal in the healthcare industry is to find a solution for combining the biological properties of the coatings with the excellent mechanical properties of traditional implant materials. Implant surfaces coated with bioactive materials promote the osseointegration of dental and orthopaedic implants. The most used bioactive coating is hydroxyapatite (HAP; $Ca_{10}(PO_4)_6(OH)_2$), which stimulates direct bone apposition and osseoconductive properties, due to its chemical similarity with bone [19–22]. HAP coatings have a high chemical reactivity in the human body, due to their dissolution rate in contact with human fluids [22–24], which is mainly dependent on their degree of crystallinity. Furthermore, there are some restrictions for usage of HAP-based bone substitutes during the surgery due to low mechanical integrity, and this could lead to failure during surgical procedures such as press-fitting or screwing [3, 4, 6, 7, 17, 25]. Usage of HAP coatings with improved mechanical and adhesive properties results in their accelerated self-adaptation in the human body, and enhances long-term performance [26, 27]. A variety of plasma-assisted techniques have been employed to obtain CaP-based coatings with desirable features including powder as well as suspension or liquid plasma spraying (PS), radio-frequency (RF) magnetron sputtering and pulsed laser deposition (PLD) [28]. Each method exhibits advantages and disadvantages, but the hydroxyapatite coating obtained by RF magnetron sputtering methods is more suitable for biomedical applications, because this technique allows us to control the coating structure (amorphous or crystalline) and the Ca/P ratio, and to obtain a uniform coating thickness with dense pore-free coating [28, 29]. Nevertheless, hydroxyapatite has two main drawbacks—poor mechanical properties and random dissolution rate in contact with human fluids —whatever the preparation method. Thus, the aim of this research is to improve the mechanical properties, and to decrease the dissolution rate of hydroxyapatite coatings, without losing its osseoconductive ability. In previous work, we showed that the mechanical properties of the sputtered HAP could be improved by Si addition, but the dissolution rate and osseointegration remained close to that of undoped HAP [30, 31]. To improve this, we propose the addition of controlled amounts of Mg to the Si doped HAP matrix. The choice of these elements was determined by the following reasons: magnesium ions are the fourth most abundant cations in mammals after sodium, potassium, and calcium; they can easily substitute the calcium in body minerals due to their chemical similarities; and they can influence the bone mineral metabolism, formation and crystallization processes [32]. Silicon, in contact with simulated body fluids (SBF), forms silanols (Si-OH) on its surface, which provide favourite sites for the migration and deposition of Ca and P ions, promoting the formation of a bone-like apatite layer, and thus favouring the attachment of osteoblasts [33–35]. It was demonstrated that the Si-OH groups are negatively charged, and promote formation of apatites such as calcium silicate, which is an amorphous calcium compound [35, 36]. Moreover, according to the literature, silicon carbide (SiC) is a bio-amorphous coating formed from two essential elements, and has a microstructure similar to that of bone. This compound promotes protein adhesion, and improves the mechanical properties of potential implant materials [37]. In our previous paper, we showed that the addition of Si improves the bioactivity and resistance of HAP in artificial saliva, thus being a good solution for dental implants [38]. Moreover, hardness and elastic modulus were increased by adding Si to the basic HAP structure [39]. Thus, it is expected that the addition of Mg to Si doped hydroxyapatite will combine the mechanical properties of HAP + Si coatings with the good osseointegration capability of Mg, thereby forming an advantageous candidate for orthopaedic implants.

2. Experimental details

2.1. Synthesis of the coatings

The coatings were prepared by RF magnetron sputtering on Si wafers and ELI-Ti6Al4V alloy (Bibus Metals CO.), using a system (AJA International) equipped with three cathodes made of stoichiometric HAP, SiC and MgO (99.9% purity, 1 inch diameter, Kurt J. Lesker Company), which worked simultaneously. Before the deposition, the substrates were sputtered using Ar^+ bombardment (1000 eV; 10 min). The deposition conditions were as presented in table 1. For this study, the deposition temperature was 700 °C, leading to crystalline HAP coatings without any post deposition annealing process [40]. Usually, the coating of HAP by RF magnetron is performed at room temperature; the coatings obtained in this way are amorphous, and need to be further annealed in order to obtain crystalline coatings [28, 40].

2.2. Microchemical, microstructural and morphological properties

The elemental composition was carried out using a scanning electron microscope (SEM) (JEOL 6060) coupled with an energy dispersive spectrometer (EDS). The structural properties were determined by x-ray diffraction (XRD) using Rietveld and

Table 1. Deposition parameters of the coatings.

Abbreviation of the coating	Base pressure ($\times 10^{-4}$ Pa)	Ar pressure ($\times 10^{-1}$ Pa)	RF powers fed (W)			Substrate bias voltage (V)	Deposition temperature (°C)
			HAP cathode	SiC cathode	MgO cathode		
SM-0	1.3	6.6	50	15		−60	700
SM-1			50	15	25		
SM-2			50	15	50		

Williamson−Hall methods. In determining XRD spectra, a Smartlab system (Rigaku, Japan) with CuK$_\alpha$ radiation was used, with 2θ range from 15 to 100° and a scan rate of 0.02° min^{-1}. Fourier transform infrared spectroscopy (FTIR) was performed using a Jasco FTIR 6300 spectrometer at a resolution of 4 cm^{-1} and 16 scans using an attenuated total reflectance (ATR) unit in order to investigate the chemical bonding in the coatings. The surface morphologies and roughness at the nanoscale level were evaluated by atomic force microscopy (AFM) (INNOVA). The tapping mode was used, in order to prevent damage to the coated surface. AFM images were acquired over an area of about $3 \times 3\ \mu\text{m}^2$.

2.3. Mechanical properties
Nanoindentation measurements were performed with a NanoTest instrument (Fischer-Cripps Lab.), equipped with a Berkovich indenter with a face angle of 65.3°. Load-unload measurements at 1.0 mN were carried out in order to determine the elastic modulus (E) and hardness (H) of the coatings. The position of each sample was randomly selected. For each measure, the holding time at the maximum load was 5 s. This time was selected to minimize the creep effect, which might influence the values of the elastic modulus and hardness. The values of H and E were averaged over 10 measurements. The values of E and H were calculated using the method described by Oliver and Pharr [41].

2.4. Electrochemical behaviour
The electrochemical behaviour of the coatings was investigated by electrochemical tests using a PARSTAT 4000 Potentiostat/Galvanostat. These tests were performed in simulated body fluid (SBF) [42] with pH = 7.2 at 37 ± 0.4 °C. The tests were conducted with a typical three-electrode cell, with saturated calomel electrode (SCE) and Pt foil as reference, working and counter electrodes, respectively. The working electrode (sample) was placed in a special Teflon sample holder in order to keep only an area of 1 cm^2 exposed to the SBF. All electrochemical measurements were carried out with a scanning rate of 0.167 mV s^{-1}, according to standard ASTM G5–94 (reapproved 1999). Also, a magnetic microstirrer (VelpScientifica) with speed range 300 rpm was used. The electrochemical tests involved the following measurement sequence:

- monitoring of the open circuit potential (OCP) for 2 h, immediately after immersion in the electrolyte;

- recording of the potentiodynamic polarization curves from −0.5 V (versus E_{OC}) to +2.5 V (versus SCE).

The electrochemical parameters were calculated as follows:

- the corrosion potential (E_{corr}) and corrosion current density (i_{corr}) were estimated by extrapolation from Tafel plots;

- the polarization resistance (R_{p}) was determined as the tangent of the curve at i = 0 from the polarization curve as a linear potential−current density plot.

The roughness parameters on a large scan length (4 mm) were analysed using a surface profilometer (Dektak 150), equipped with a low-inertia stylus sensor (12.5 mm radius). At least ten profiles were assessed in different areas of each sample. The R_{a} (average roughness) and R_{q} (root mean square roughness) parameters were calculated for all the coatings, before and after electrochemical tests.

All collected data are presented as mean standard deviations (SD), being statistically analysed by paired Student's t-test, with $\alpha = 0.05$.

2.5. Biological experiments
Human osteogenic sarcoma cells (SaOS-2) were purchased from the American Type Tissue Collection (ATCC HTB 85), and cultured in 85% McCoy's 5A medium, supplemented with 15% fetal bovine serum and 1% penicillin/streptomycin at 37 °C and 5% CO$_2$. Cells at densities either 10 000 (3 day exposure) or 15 000 (1 day exposure) cells cm^{-2} were seeded onto coated and uncoated Ti6Al4V discs (15 mm diameter, 1 mm thick). The medium was changed every second day.

Cell viability was assessed by live/dead fluorescence staining using calcein-AM (Invitrogen, USA) and propidium iodide (PI, Sigma, USA). On the first and third day after seeding, cells were washed with HEPES buffered saline (HBSS) and stained with calcein-AM (2 μM) and PI (4 μM) in HBSS for 30 min at room temperature (RT) in the dark. Thereafter, the staining solution was removed, and samples were

Table 2. Elemental composition of the coatings; mean of values obtained in three different points.

Coating	Elemental composition (at.%)					(Ca+Mg)/P
	Ca	P	Si	Mg	Ti	
SM-1	8.5 ± 0.06	5.1 ± 0.08	6.6 ± 0.3	0.8 ± 0.02	balance	1.82
SM-2	8.2 ± 0.05	4.9 ± 0.05	5.4 ± 0.2	1.9 ± 0.02	balance	2.01
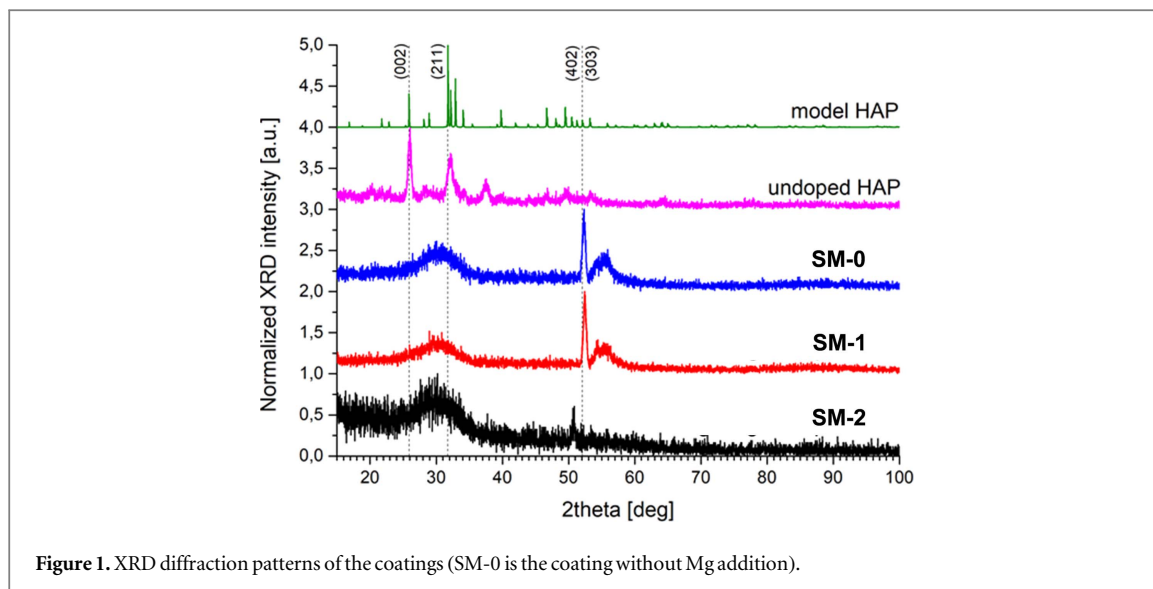
Figure 1. XRD diffraction patterns of the coatings (SM-0 is the coating without Mg addition).

mounted upside down into coverslip bottom dishes (SPL, Korea) using a drop of ProLong Diamond anti-fade solution (Molecular Probes, USA). Samples were immediately photographed, and analyzed with Axio-vision software and an Axiovert 200 microscope (Zeiss, Germany), using appropriate filters. At least five random microscopic visual fields for each sample surface were analyzed for cell counts. Cell morphology was determined after day 1 or 3 of culture. Cells were washed with phosphate buffered saline (PBS), fixed with 4% formalin (5 min, RT), permeabilized using 0.5% Triton X-100 (6 min, RT), and incubated with 1% bovine serum albumin in PBS (10 min, RT) to block unspecific bindings. After washing with PBS, cells were incubated with 0.1 μM of phalloidin-TRITC (Sigma, USA) for one hour at RT to detect actin filaments. Thereafter, cells were washed three times with PBS. Cell nuclei were visualized by means of incubation with 1 μg ml^{-1} DAPI (Sigma, USA) for 5 min at RT. Images of cells growth on samples were acquired with a fluorescence microscope (Zeiss, Germany), using appropriate filters.

3. Results and discussions

3.1. Elemental composition and chemical bonding
The EDS measurements were performed at three points of each sample. The averaged EDS values of the coatings are given in table 2. The Mg doped hydroxyapatite coating can be written as $Ca_{10-x}Mg_x(PO_4)_6(OH)_2$. For

Table 3. Structural data determined from XRD spectra using Rietveld and Williamson$-$Hall methods: a_0, c_0—lattice constants, γ_0—angle between cell edges, CDD—the size of the coherently-diffracting domains, ε—relative lattice strains.

Sample	a_0 (Å)	c_0 (Å)	γ_0 (^{0})	CDD (Å)	ε (%)
HAP-model (theory)	9.426	6.880	120	—	—
Undoped HAP	9.526	6.856	120	630	0.896
SM-0	9.494	6.780	120	100	-0.181
SM-1	9.526	6.880	120	110	-0.201
SM-2	9.463	6.791	120	110	-0.209

this reason, the (Ca+Mg)/P ratio was calculated, and is presented in table 2. It was found that (Ca+Mg)/P ratio of the prepared coatings is higher than the stoichiometric ratio of undoped hydroxyapatite (Ca/P = 1.67). As evidence of the effect of Mg addition into Si doped HAP, the XRD results are presented below (figure 1). As expected, the amount of Mg increased by increasing RF power fed to the MgO cathode. At higher power, the Mg content is more than doubled. It is worth mentioning that we intended to keep Mg at a low content in the coatings, in order to limit its effect on the dissolution rate in corrosive human solution, and to improve the biological capability of the coatings.

The XRD spectra of the investigated coatings are illustrated in figure 1. The structural data determined from XRD spectra using Rietveld and Williamson $-$Hall methods are shown in table 3. Results on the

unit cell geometry of various HAP structures obtained using the Rietveld refinement method together with the Williamson–Hall plot suggest that the doping process reasonably influences geometry of the lattice structure. Pure HAP crystal appears similar to the theoretical structure, because the diffraction reveals several relatively sharp peaks considering, for instance, (002) and (211) reflexes. The size of coherently-diffracting domains (CDD) exceeds 600 nm, and is found to be the largest among the samples under study. Unlike the remaining samples, its relative microstructural strains also turn out to be tensile at the level of 0.9%, which demonstrates cell elongation within the $x-y$ plane. The diffraction spectra were analysed in the reduced range from 15° to 100°, in order to remove several low-angle peaks of unknown origin.

Doping with silicon decreases the size of CDD domains to a value of 100 nm, i.e. by a factor of 6. Simultaneously, Si doped HAP appears to be more disordered, because of observed very broad XRD peak at around 30°, in place of the previous sharp (002) and (211) peaks. Also important is that the substitution of atoms in the HAP structure with Si results in contraction of the unit cell, compared with undoped HAP. Both lattice constants are smaller than in undoped HAP, and the microstrains are found compressive.

Sample SM-2, and also—to a lesser degree—the remaining samples doped with silicon, exhibit significant background in their XRD spectra, which might be due to several factors. First of all, one needs to consider diffuse scattering due to various crystallite imperfections. Short-range ordered material with CDD domains not larger than around 100 nm could be a source of intense scattering. On the other hand, the very sharp and intense peak at 52° suggests the opposite. This peak is characteristic of highly-ordered granular material, with preferred orientations of the polycrystals of which it is made. In this case, however, one should expect larger grains of the HAP material, which suggests that the CDD domains might form texturized mosaic hyperstructures. On the whole, the HAP structure appears to be a mixture of disordered and crystalline phases.

Additional doping with Mg further influences the crystalline structure of the Si doped HAP. Compared to the theoretical structure, the lattice constants in Mg- and Si doped HAP are found larger within the $x-y$ plane, but lower along the z axis. Despite these small variations in the lattice parameters, the overall microstrains are found more compressive, which indicates progressive lattice contraction. The size of the CDD domains remains untouched at around 100 nm. Note that the sharp peak at 52° is still seen in lightly Mg doped coatings, but disappears in that heavily doped. The XRD data showed that the Mg and Si addition into HAP lead to amorphisation, an effect related to the nucleation growth, leading to the decrease of grain size.
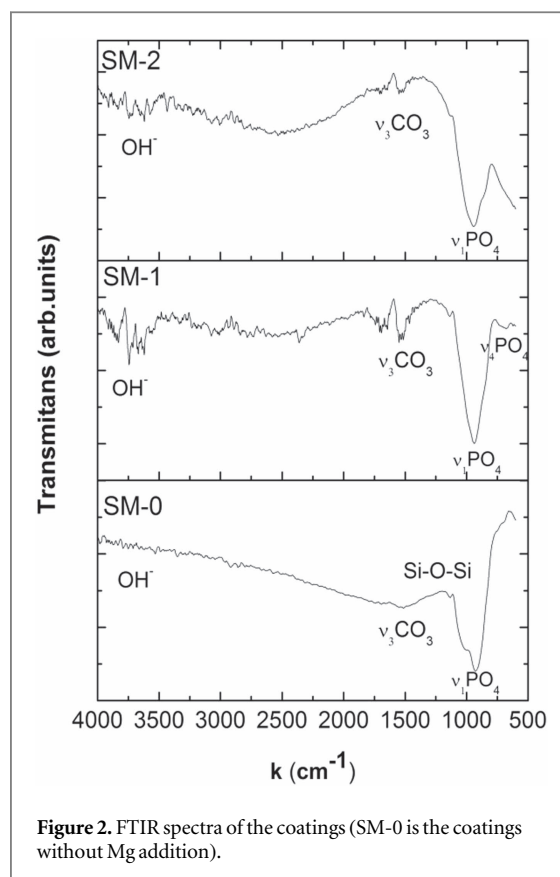

Figure 2. FTIR spectra of the coatings (SM-0 is the coatings without Mg addition).

The FTIR spectra of SM-1 and SM-2 coatings indicated the presence of characteristic IR absorption bands which can be attributed to CaP coatings (figure 2). The absorption bands at 939 and 680 cm^{-1} correspond to asymmetric stretching ($\nu 1$) and bending ($\nu 4$) vibrations of PO$_4^{3-}$. As depicted in figure 2, the presence of the absorption bands from 3900 to 3400 cm^{-1} can be assigned to the hydroxyl groups (OH$^-$), while the weak absorption bands located between 1600 and 1480 cm^{-1} were associated to the CO$_3^{2-}$ vibration mode. In a previous paper, we showed that the Si doped HAP coating exhibited bands attributed to HAP phase at 682 cm^{-1}, 962 cm^{-1}, and a low one at 1045 cm^{-1}, indicating that the Si addition does not affect the formation of HAP phase [39]. Also, weak bands at 1528 cm^{-1} and 3553 cm^{-1} were found, attributed to CO$_3^{2-}$ and hydroxyl bands, respectively. Incorporation of more magnesium content into Si doped HAP coatings lead to an intensity change of CO$_3^{2-}$ and OH$^-$ absorption bands. Further, the $\nu 1$-PO$_4^{3-}$ band structure at 939 cm^{-1} was changed, indicating a possible modification of HAP structure as a consequence of Mg addition in the Si doped HAP structure.

3.2. Morphology and topography

Figure 3 shows the AFM 3D images. The coatings without Mg addition (SM-0) are presented for comparison. As depicted in figure 3, all of the coatings exhibited smooth surfaces and uniform growth. The roughness parameters calculated from the AFM
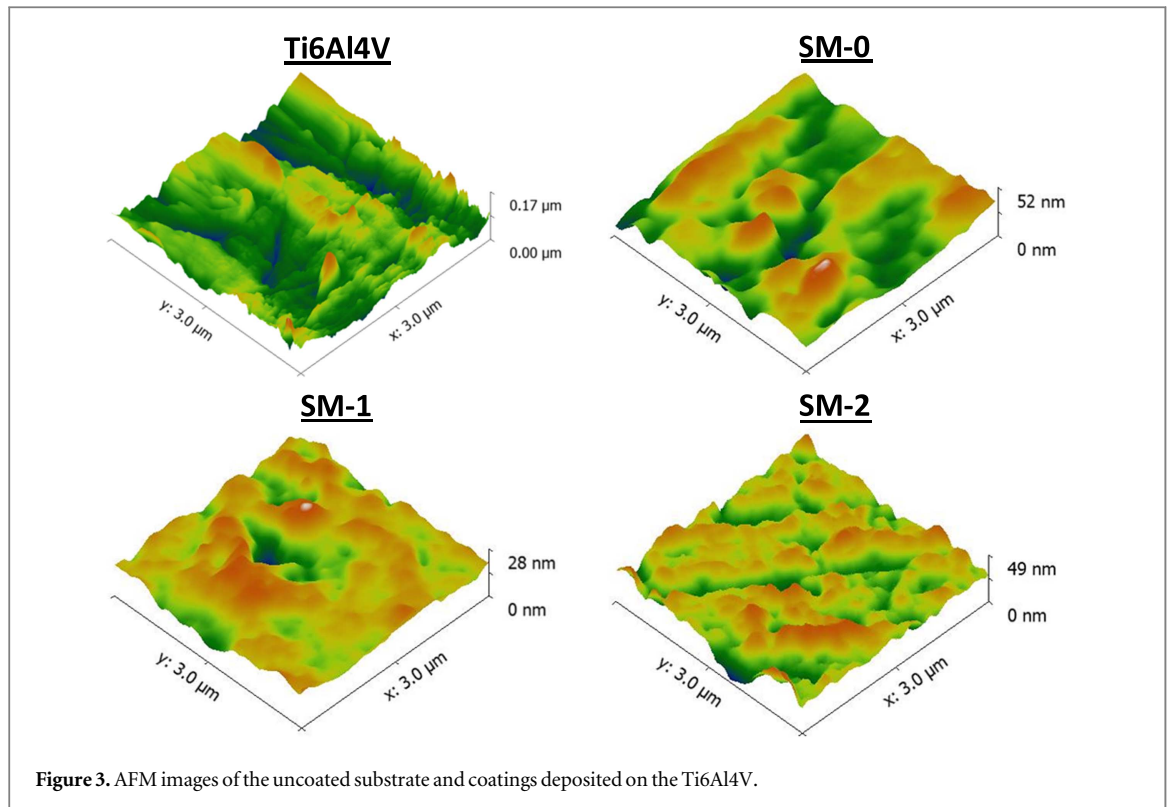
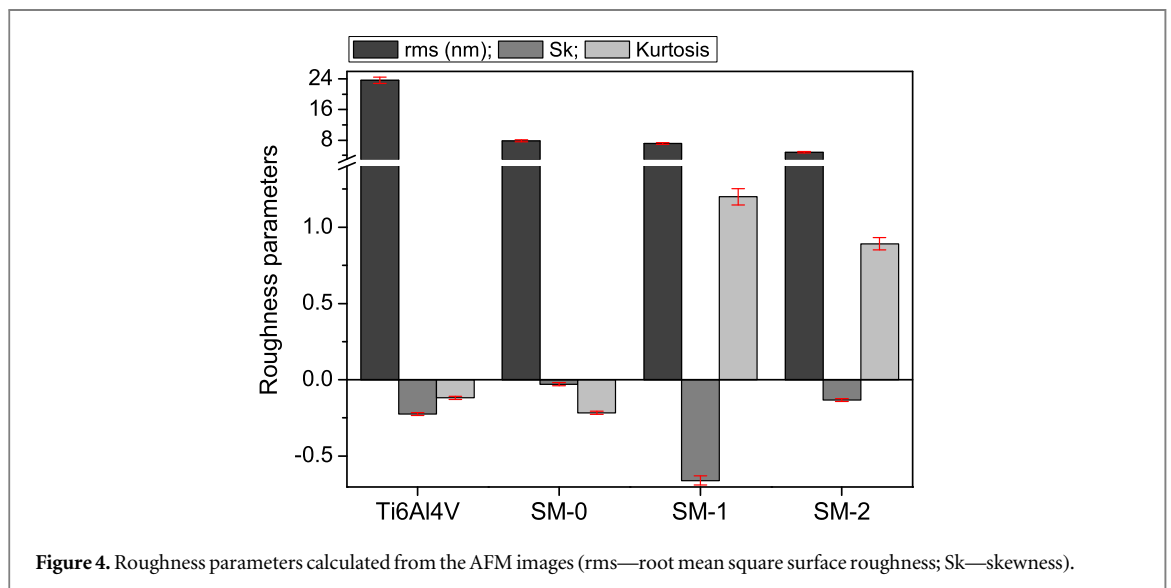**Figure 3.** AFM images of the uncoated substrate and coatings deposited on the Ti6Al4V.

Figure 4. Roughness parameters calculated from the AFM images (rms—root mean square surface roughness; Sk—skewness).

images are illustrated in figure 4. The uncoated substrate exhibited an rms roughness of about 23.7 nm. The roughness of the coating without Mg addition is 7.8 nm. One may see that the surface roughness of the coatings was decreased by Mg addition (SM-1 = 7.1 nm and SM-2 = 4.8 nm). The coating with small Mg content has a smooth surface, indicating that the increasing RF power fed to the Mg cathode led to a slight increase in roughness. The flat surfaces presented skewness close to zero. If the skewness has negative value, it can be said that the surface consists of many valleys. Figure 4 shows that all of the coatings as well as the uncoated substrate have a negative skewness. The valleys found on the uncoated

substrates are due to the polishing process. The coating process covers most of the substrate valleys obtained during the polishing process, leading to a uniform distribution on the uncoated substrate.

Experimental data that follow a perfectly normal distribution have a kurtosis value of zero. Those data which deviate from zero indicate that roughness is not normally distributed. The uncoated substrate has a negative kurtosis value, proving that the surface has some grooving, probably due to the polishing process. Also, the coating without Mg addition has a negative kurtosis value. Both Mg doped coatings exhibited a positive kurtosis value. In the literature, it is reported that the surfaces with few high peaks and low valleys

Table 4. Mechanical properties of HAP-Si coatings with and without Mg addition at 1.0 mN applied load.

Coating	Load (mN)	E (GPa)	H (GPa)	H/E	H^3/E^2
SM-0	1.0	114.9 ± 0.6	12.1 ± 0.3	0.1054	1.3432
SM-1	1.0	98.3 ± 1.2	10.4 ± 0.3	0.1055	1.1538
SM-2	1.0	52.9 ± 1.5	5.5 ± 0.2	0.1046	0.6060

showed a kurtosis of less than 3, and of more than 3 for surfaces with higher peaks and low valleys [43]. The coating SM-1 demonstrated a high positive kurtosis (3.02), meaning that on the surfaces of coatings few high peaks and low valleys are seen compared with the SM-2 surface (1.14).

Skewness and kurtosis are two roughness parameters which influence the corrosion and friction performance of a material. More positive values of skewness indicate good corrosion resistance, while negative skewness can lead to pitting corrosion, as indicated in the literature [44]. According to this fact, one may observe that SM-2 having more positive skewness than SM-1 probably indicates a better corrosion resistance.

3.3. Mechanical properties

In our previous study, it is reported that RF power fed to the SiC target has an enhanced effect on the mechanical properties of HAP-Si coatings, and optimum results are obtained at 1.0 mN [39]. Therefore, in this study load −unload measurements at 1.0 mN were performed. The maximum penetration depth is smaller for the HAP-Si coating without Mg addition (SM-0), suggesting that Mg addition does not have any remarkable influence on the mechanical properties of HAP-Si coatings.

The experimental values of mean hardness, H, mean elastic modulus, E, H/E and H^3/E^2 ratios obtained from the nanoindentation testing of SM-0, SM-1 and SM-2 coatings are presented in table 4. It is observed that both hardness and elastic modulus of the coated samples decrease with Mg addition. The SM-2 sample exhibited low elastic modulus (52 GPa), being more or less closer to that of human bone (maximum 20 GPa) [45].

Although hardness has long been regarded as a primary material property which defines wear resistance, there is strong evidence to suggest that the elastic modulus can also have an important influence on wear behaviour. In particular, the elastic strain to failure, which is related to the ratio of hardness (H) and elastic modulus (E), has been shown by a number of authors to be a more suitable parameter for predicting wear resistance than is hardness alone.

It is recognized by many authors that the ranking of materials according to their H/E ratio can provide extremely close agreement to their ranking in terms of wear. The ratio between H and E (H/E ratio) is called the 'plasticity index', and it was first used as a material

ranking parameter by Oberle [46, 47], as a valuable measure in determining the limit of elastic behaviour in a surface contact, which is clearly important to describe the 'elastic strain to failure'. H^3/E^2 should also be a strong indicator of a coating's resistance to plastic deformation. This ratio is indicative of the material's elasticity, high values of H^3/E^2 reflecting a predominantly elastic behaviour [48].

The results shown in table 4 reveal the Mg content in HAP-Si coating structure to have an insignificant effect on the H/E ratio; both HAP+SiC+Mg coatings exhibited H/E ratio similar to that of HAP+SiC. Concerning the H^3/E^2 ratio, SM-0 proved to have a more elastic behaviour during loading than that of Mg doped coatings—indicative of good wear resistance. Comparing the Mg doped coatings, the SM-1 surface shows high H^3/E^2 ratio, predicting a good wear resistance.

3.4. Electrochemical behaviour

Open circuit potential measurement was carried out for 2 h in SBF solution (figure 5(a)). The potentiodynamic curves of the uncoated substrate and the coatings are presented in figure 5(b). The electrochemical parameters are presented in table 5. The results can be summarized as follows:

- Both the coatings exhibited similar E_{oc} potential values, and they are slightly more electronegative than those of the uncoated substrate, as is seen in figure 5(a).

- The E_{oc} potential of both coatings started to gradually increase, indicating that a protective layer was formed on the surfaces. The uncoated surface does not exhibit any significant change in E_{oc} during the test, demonstrating that the protective layer formed is stable.

- SM-2 coating exhibited large fluctuations of current density in the anodic branch during the potentiodynamic tests. Fluctuation in the current density may be attributed to the sequential effect of protection process and further dissolution aggravated by the increase in potential. This phenomenon is observed for SM-1 coating at low potential values, settling rapidly.

- Potentiodynamic polarization curves for both coatings have passivation domain, being more evident for SM-1 (0.2–1.2 V), indicating that this coating is able to resist SBF corrosive attack.
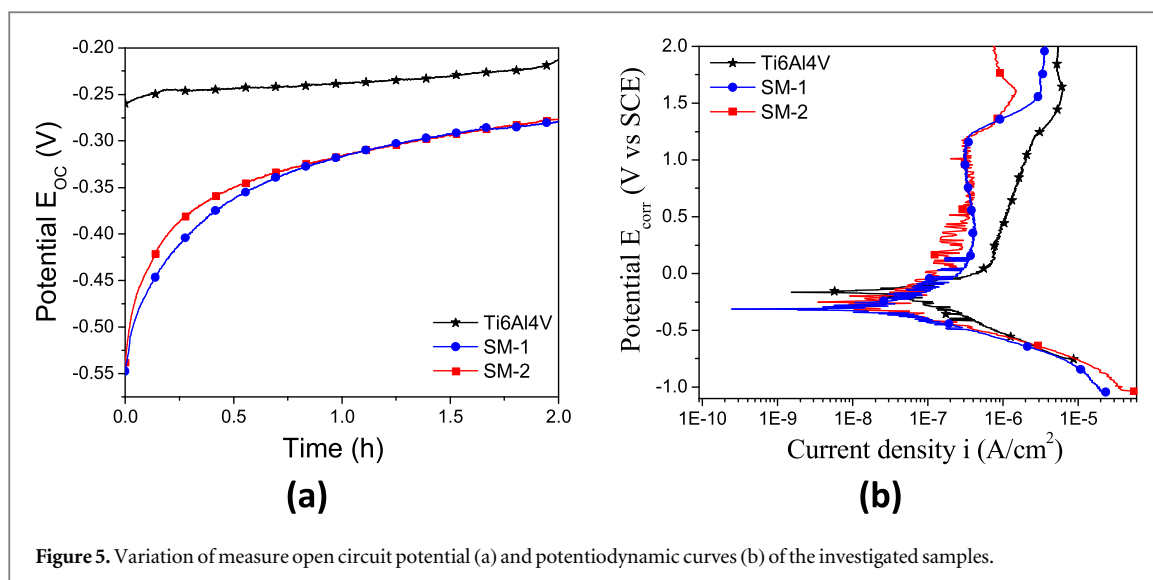
Figure 5. Variation of measure open circuit potential (a) and potentiodynamic curves (b) of the investigated samples.

Table 5. Electrochemical parameters of the investigated samples: corrosion potentials (E_{corr}), corrosion current density (i_{corr}), polarization resistance (R_p).

Sample	E_{corr} (mV)	i_{corr} (nA cm^{-2})	R_p (kΩ)
Ti6Al4V	−163.1	46.068	1032
SM-1	−305.8	34.920	1563
SM-2	−300.5	38.779	1504

- Comparing the electrochemical parameters, both coatings improved the corrosion resistance compared to uncoated substrate.

- Comparing the coatings, the SM-2 showed a higher electropositive E_{corr} value.

- SM-1 coatings have high polarization resistance and low corrosion current density.

It is well known that a material with a higher electropositive E_{corr}, low i_{corr}, and high R_p display a good corrosion resistance [49, 50]. Both coatings showed the superior corrosion resistance compared to the uncoated substrate. It can be seen that the SM-1 exhibited low i_{corr} and high R_p, indicating better corrosion resistance in SBF solution. This conclusion is also in good agreement with the AFM results, which showed the SM-1 sample to have positive values of skewness—that can indicate good corrosion resistance.

3.5. Mass loss rate and roughness on large area after electrochemical tests

In order to evaluate the effect of the electrochemical tests on the investigated surfaces, the mass loss rate and roughness of the coatings and uncoated alloy after corrosion tests were calculated. The mass loss rate (*MR*) was determined by weight loss technique, the samples were weighed before and after electrochemical tests and *MR* was calculated using the formula

$$MR = (w_1 - w_2)/(A \times d) \quad (\text{mg cm}^{-2}/\text{day})$$

where w_1 is mass before the electrochemical tests (mg), w_2 is mass after the electrochemical tests (mg), A is exposed specimen area (cm^2), d is the duration of the electrochemical tests (days).

The mass loss rates of the uncoated substrate and, coatings are presented in figure 6. The results of the coatings without Mg addition are also presented for comparison, results reported in the study of Ak Azem *et al* [30]. It is observed that the coatings significantly decreased the mass loss rate of Ti6Al4V alloy. The addition of the Mg in Si doped HAP led to a decrease in mass loss rate, indicating a better resistance to corrosive attack. It can be seen from figure 6 that the mass loss rate of the coatings increases with increasing Mg content. From the point of view of the mass loss rate of the coatings, SM-1 has low dissolution rate compared to SM-2 and SM-0.

The surface roughness parameters of the samples on scan length of about 4 mm, before and after electrochemical tests, were presented in figure 7. It has been found that surface profilometry measurement results are consistent with the AFM analysis results. AFM analysis results showed that the substrate surface became smoother with coating process and the SM-1 coating is smoother than the SM-2 (figures 3 and 4). The R_a and S_k values of coatings decreased after corrosion testing, being attributed to a presence of dissolution phenomena during the electrochemical tests which is uniform on entire surface. The roughness and mass loss rate results confirm the electrochemical ones: respectively, the SM-1 samples have better corrosion resistance in SBF solution and small dissolution of coating.

3.6. Biological properties

Bone cell adhesion and morphology were investigated by plating SaOS-2 cells directly on standard titanium alloy (Ti6Al4V) and the coated surfaces (figure 8). After day 1, attached live cell numbers were higher on
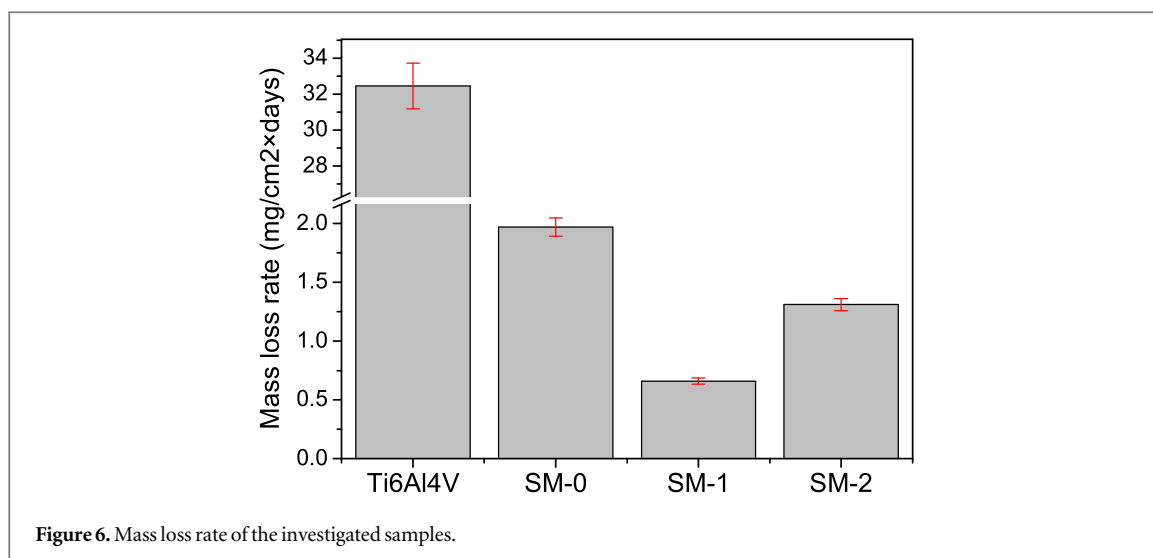
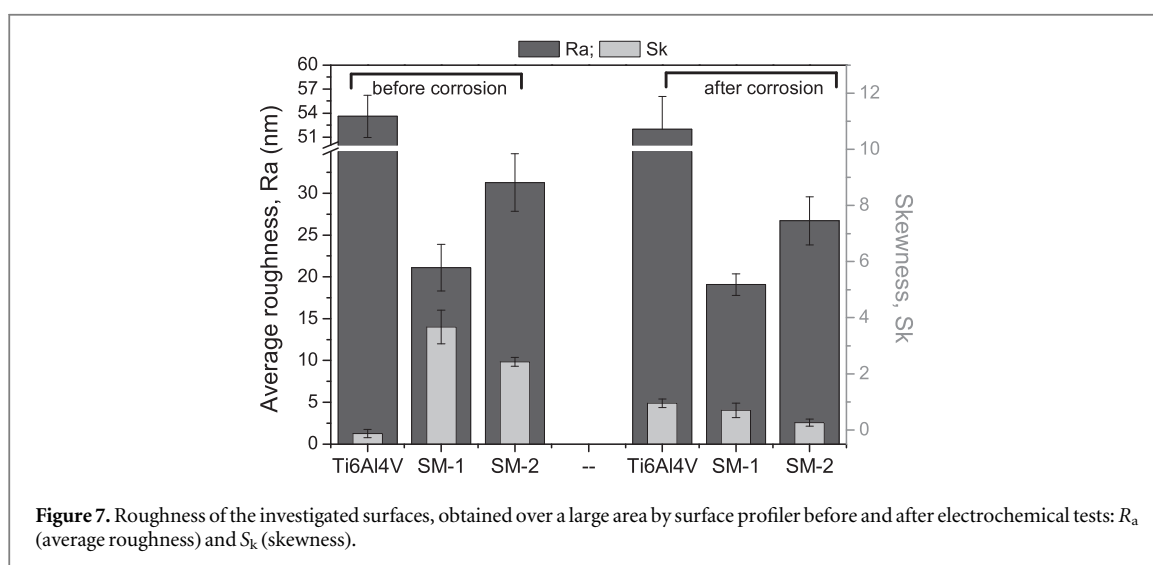**Figure 6.** Mass loss rate of the investigated samples.

Figure 7. Roughness of the investigated surfaces, obtained over a large area by surface profiler before and after electrochemical tests: R_a (average roughness) and S_k (skewness).

Ti6Al4V alloy, but significantly lower on the coatings (table 6). SaOS-2 osteoblasts displayed their typical polygonal shape with prominent actin stress fibres visible on uncoated alloy and SM-1. In contrast, cells on the SM-2 coating were less spread, thus smaller in size and the formation of actin fibres was less developed. After day 3, cell numbers almost doubled on TiAl4V and SM-1, demonstrating active bone cell proliferation. Again, numbers of cells grown on SM-2 were considerably lower. Actin cytoskeleton appeared best developed on SM-1, followed by standard alloy and SM-2.

Cell viability after day 1 or 3 in direct contact with standard alloy or the coated surfaces was investigated by means of live/dead fluorescence staining. Figure 9 shows that almost all cells were vital (green), with only very few dead cells (red, arrows) detected. The live/dead assay also showed significantly more attached and living cells per microscopic view on the Ti6Al4V surface than on the coatings. The same parameter is significantly higher on SM-1 coating when compared

to the SM-2 surface. As such, this data supports the outcome of the adhesion test.

Our findings are supported by data from Wagener *et al* [51] who demonstrated that MG63 osteosarcoma cells showed lower cell numbers and inhibited cell spreading when seeded directly on pure magnesium or on differently coated Mg. It was reported that the local rise in Mg level does not seem to have a significant impact on osteosarcoma cell proliferation [31, 51]. High Mg levels can, however, inhibit deposition of Ca phosphate mineral matrix [52]. Deposition of mineral matrix is a crucial step in bone formation and healing. We demonstrated that the SM-2 coatings possess less corrosion resistance than SM-1, hence osteoblast seeded on SM-2 coatings will be more affected by hydrogen evolution, and thus should attach and proliferate more slowly. This may explain the low attachment and growth rate of SaOS-2 osteoblasts on SM-2 coatings described in this paper.

Calcium ions can be partially substituted with magnesium ions in the body. More than 60% of total Mg is stored in bones, and a strong association
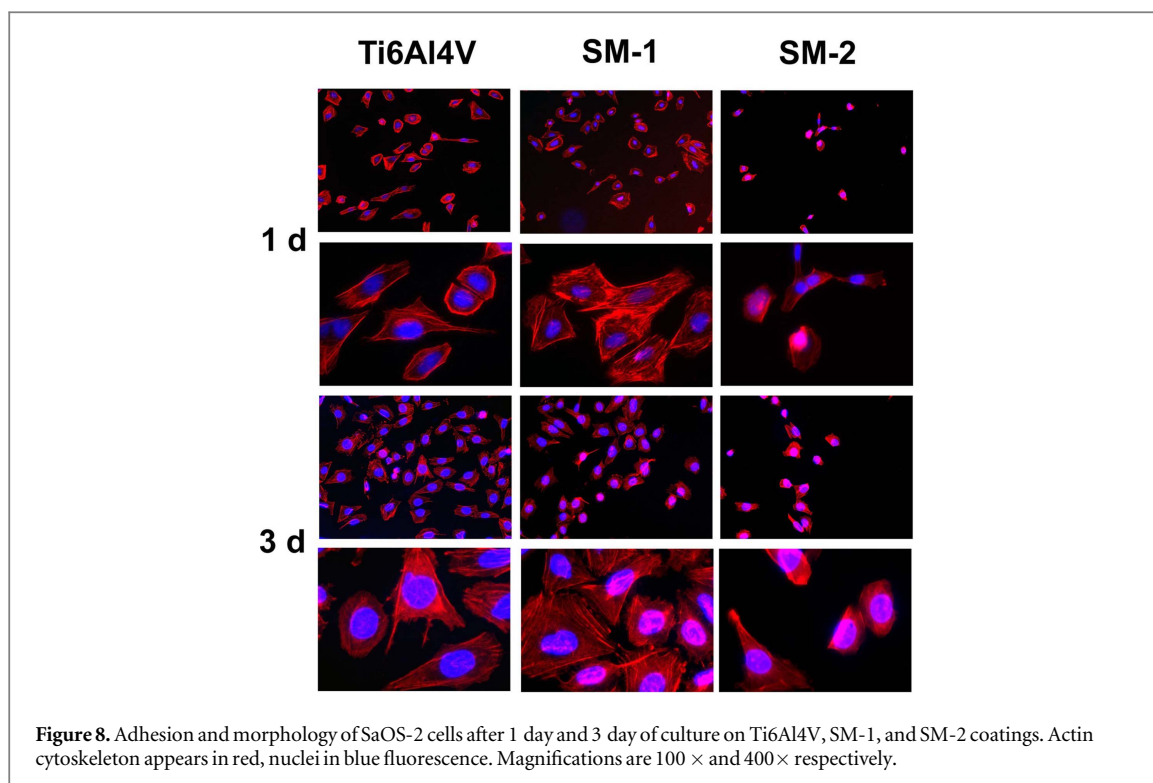
Figure 8. Adhesion and morphology of SaOS-2 cells after 1 day and 3 day of culture on Ti6Al4V, SM-1, and SM-2 coatings. Actin cytoskeleton appears in red, nuclei in blue fluorescence. Magnifications are $100 \times$ and $400\times$ respectively.

Table 6. Relative numbers of living cells after 1 and 3 days of culture. The different superscript letters within each column indicate the *p* value.

Surface	1 d	3 d
Ti6Al4V	42.33 ± 6.15^{a}	81.83 ± 13.35^{a}
SM-1	27.50 ± 3.45^{b}	56.83 ± 23.03^{b}
SM-2	15.83 ± 2.04^{c}	22.17 ± 5.15^{c}

between bone density and Mg intake has been found. Yet Mg can also antagonize Ca, and may thereby affect Ca-dependent cell functions. A diet low in Mg promotes osteoporosis in rodents and humans. This results, *inter alia*, from decreased bone formation, due to lower osteoblast numbers and activity enhanced osteoclast proliferation. Also, elevated Mg levels seem to negatively influence bone metabolism, and thus have a harmful effect on osteoblast function and bone health [53].
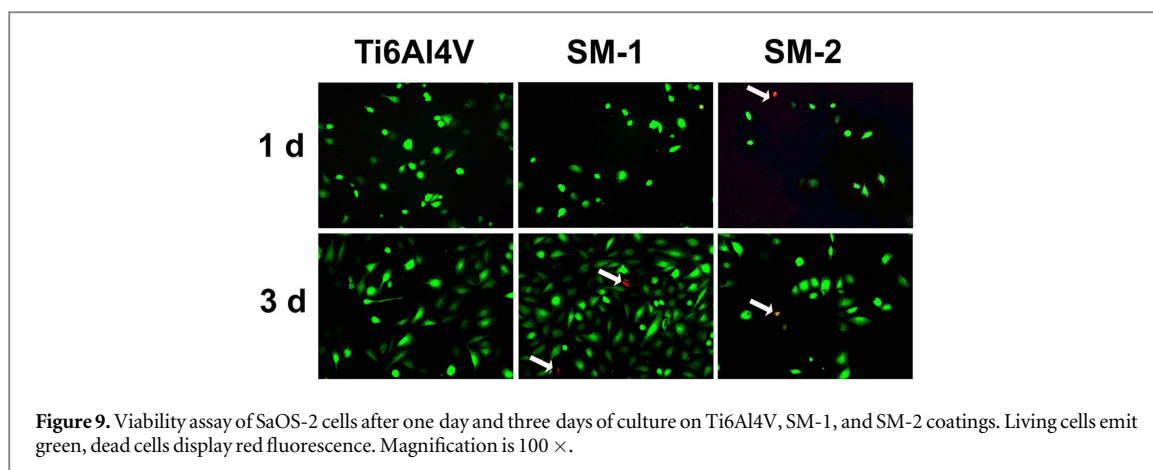
4. Conclusions

In this study, Si and Mg doped hydroxyapatite coatings were prepared on Ti6Al4V alloy substrates, using magnetron sputtering. The results can be summarized as follows:

- Si and Mg addition does not influence the formation of a hydroxyapatite phase.

- Both hardness and elastic modulus of the coated samples decrease with Mg addition in the Si doped HAP structure.

- Both doped HAP coatings were found to enhance the corrosion resistance of the Ti6Al4V alloy in the SBF solution at human body temperature. The best corrosion resistance was found for the coatings prepared with low RF power fed to the MgO cathode (25 W), which also proved to have a smooth surface.

- The addition of the Mg and Si doped HAP led to a decrease in mass loss rate, indicating a low degradation rate in contact with SBF solution. The coatings with low Mg content have low mass loss rate compared to those with high Mg content.

- All the coatings were biocompatible as demonstrated by SaOS-2 bone cells attachment and growth. Compared to Ti6Al4V alloy, however, cell numbers were significantly lower on both coatings. Also, cell proliferation and morphology were inferior on samples with the high Mg contents.

Based on these results, the incorporation of both Mg and Si into the structure of HAP could be a promising way to prepare implantable surfaces suitable for bone substitution. The present paper showed that the mechanical properties, corrosion resistance and degradation rate of hydroxyapatite can be significantly improved, in detriment of cell proliferation and morphology characteristics. All of the coatings promoted bone cell attachment and growth, but the cell numbers were significantly lower on both coatings than on uncoated alloy. For this reason, we believe that further studies should be developed for investigation of the interaction between cells and coated surfaces.

Figure 9. Viability assay of SaOS-2 cells after one day and three days of culture on Ti6Al4V, SM-1, and SM-2 coatings. Living cells emit green, dead cells display red fluorescence. Magnification is 100 ×.

Acknowledgments

ORCID iDs

Cosmin Mihai Cotrut https://orcid.org/0000-0002-8991-7485

References

[1] Karlsson K H, Ylänen H and Aro H 2000 Porous bone implants *Ceram. Int.* **26** 897–900

[2] Matassi F, Botti A, Sirleo L, Carulli C and Innocenti M 2013 Porous metal for orthopedics implants *Clin. Cases Miner. Bone Metab.* **10** 111–5

[3] Ros V, Martínez Alvarez M, Fernández S, Girvent R, Carballo A, Gili G and Torner P 2014 High short-term loosening rates with the wagner standard cup *J. Arthroplasty* **29** 172–5

[4] Beckmann N A, Weiss S, Klotz M C M, Gondan M, Jaeger S and Bitsch R G 2014 Loosening after acetabular revision: Comparison of trabecular metal and reinforcement rings. A systematic review *J. Arthroplasty* **29** 229–35

[5] Bosco R, Van Den Beucken J, Leeuwenburgh S and Jansen J 2012 Surface engineering for bone implants: a trend from passive to active surfaces *Coatings* **2** 95–119

[6] Damm N B, Morlock M M and Bishop N E 2015 Friction coefficient and effective interference at the implant-bone interface *J. Biomech.* **48** 3517–21

[7] Rancourt D, Shirazi-Adl A, Drouin G and Paiement G 1990 Friction properties of the interface between porous-surfaced metals and tibial cancellous bone *J Biomed Mat Res* **24** 1503–19

[8] Chanlalit C, Shukla D R, Fitzsimmons J S, An K N and O'Driscoll S W 2012 Stress shielding around radial head prostheses *J. Hand Surg. Am.* **37** 2118–25

[9] Sumner D R and Galante J O 1992 Determinants of stress shielding: design versus materials versus interface *Clin Orthop Relat Res* **274** 202–12

[10] Niinomi M and Nakai M 2011 Titanium-based biomaterials for preventing stress shielding between implant devices and bone *Int. J. Biomater.* **2011** 836587

[11] Sumner D R 2015 Long-term implant fixation and stress-shielding in total hip replacement *J. Biomech.* **48** 797–800

[12] Chang J K, Chen C H, Huang K Y and Wang G J 2006 Eight-year results of hydroxyapatite-coated hip arthroplasty *J. Arthroplasty* **21** 541–6

[13] Goyenvalle E, Aguado E, Nguyen J M, Passuti N, Le Guehennec L, Layrolle P and Daculsi G 2006 Osteointegration of femoral stem prostheses with a bilayered calcium phosphate coating *Biomaterials* **27** 1119–28

[14] Lee I-S, Kim H-E and Kim S-Y 2000 Studies on calcium phosphate coatings *Surf. Coatings Technol.* **131** 181–6

[15] LaPorte D M, Mont M A and Hungerford D S 1999 Proximally porous-coated ingrowth prostheses: limits of use *Orthopedics* **22** 1154–60

[16] Reynolds T 2016 National institute of arthritis and musculoskeletal and skin diseases (NIAMS): questions and answers about hip replacement (NIH Publication No. 16-4907) (National Institute of Arthritis and Musculoskeletal and Skin Diseases)

[17] Bishop N E, Höhn J C, Rothstock S, Damm N B and Morlock M M 2014 The influence of bone damage on press-fit mechanics *J. Biomech.* **47** 1472–8

[18] Hedia H S and Fouda N 2014 Design optimization of cementless hip prosthesis coating through functionally graded material *Comput. Mater. Sci.* **87** 83–7

[19] Nayak A K 2010 Hydroxyapatite synthesis methodologies: An overview *Int. J. ChemTech Res.* **2** 903–7

[20] Orlovskii V P, Komlev V S and Barinov S M 2002 Hydroxyapatite and hydroxyapatite-based ceramics *Inorg. Mater.* **38** 973–84

[21] Sadat-Shojai M, Khorasani M T, Dinpanah-Khoshdargi E and Jamshidi A 2013 Synthesis methods for nanosized hydroxyapatite with diverse structures *Acta Biomater.* **9** 7591–621

[22] Shepherd J H, Friederichs R J and Best S M 2015 *Hydroxyapatite (Hap) for Biomedical Applications* ed M Mucalo (Cambridge: Elsevier)

[23] Queiroz A C, Santos J D, Monteiro F J and Prado da Silva M H 2003 Dissolution studies of hydroxyapatite and glass-reinforced hydroxyapatite ceramics *Mater. Charact.* **50** 197–202

[24] Fulmer M T, Ison I C, Hankermayer C R, Constantz B R and Ross J 2002 Measurements of the solubilities and dissolution rates of several hydroxyapatites *Biomaterials* **23** 751–5

[25] Chen C M, Cheng C T, Lin C S, Lin S C, Chiang C C, Luo C A and Tseng C S 2014 Biomechanical effects of bone-implant fitness and screw breakage on the stability and stress performance of the nonstemmed hip system *Clin. Biomech.* **29** 161–9

[26] Janković A, Eraković S, Vukašinović-Sekulić M, Mišković-Stanković V, Park S J and Rhee K Y 2015 Graphene-based antibacterial composite coatings electrodeposited on titanium for biomedical applications *Prog. Org. Coatings* **83** 1–10

[27] Duminis T, Shahid S and Hill R G 2017 Apatite glass-ceramics: a review *Front. Mater.* **3** 1–15

[28] Surmenev R A 2012 A review of plasma-assisted methods for calcium phosphate-based coatings fabrication *Surf. Coatings Technol.* **206** 2035–56

[29] Surmenev R A, Surmeneva M A and Ivanova A A 2014 Significance of calcium phosphate coatings for the enhancement of new bone osteogenesis—A review *Acta Biomater.* **10** 557–79

[30] Azem F A, Kiss A, Birlik I, Braic V, Luculescu C and Vladescu A 2014 The corrosion and bioactivity behavior of SiC doped hydroxyapatite for dental applications *Ceram. Int.* **40** 15881–7

[31] Leidi M, Dellera F, Mariotti M, Banfi G, Crapanzano C, Albisetti W and Maier J A M 2012 Nitric oxide mediates low magnesium inhibition of osteoblast-like cell proliferation *J. Nutr. Biochem.* **23** 1224–9

[32] Becker A, Ziegler A and Epple M 2005 The mineral phase in the cuticles of two species of Crustacea consists of magnesium calcite, amorphous calcium carbonate, and amorphous calcium phosphate *Dalton Trans.* **10** 1814–20

[33] Boccaccini A R, Brauer D S and Hupa L 2016 *Bioactive Glasses: Fundamentals, Technology and Applications* (Cambridge: Cambridge Royal Society Of Chemistry)

[34] Dorozhkin S V 2009 Calcium orthophosphate-based biocomposites and hybrid biomaterials *J. Mater. Sci.* **44** 2343–87

[35] Dorozhkin Sergey V 2016 *Calcium Orthophosphate-Based Bioceramics and Biocomposites* (Weinheim: Wiley-VCH)

[36] Balani K, Verma V, Agarwal A and Narayan R 2015 Biosurfaces: a materials science and engineering perspective *Intergovernmental Panel on Climate Change* (Hoboken, NJ: Wiley) pp 1–392

[37] Will J, Hoppe A, Müller F A, Raya C T, Fernández J M and Greil P 2010 Bioactivation of biomorphous silicon carbide bone implants *Acta Biomater.* **6** 4488–94

[38] Vranceanu D M *et al* 2016 Osseointegration of sputtered SiC-added hydroxyapatite for orthopaedic applications *Ceram. Int.* **42** 10085

[39] Vladescu A, Birlik I, Braic V, Toparli M, Celik E and Ak Azem F 2014 Enhancement of the mechanical properties of hydroxyapatite by SiC addition *J. Mech. Behav. Biomed. Mater.* **40** 362–8

[40] Vladescu A, Braic M, Azem F A, Titorencu I, Braic V, Pruna V, Kiss A, Parau A C C and Birlik I 2015 Effect of the deposition temperature on corrosion resistance and biocompatibility of the hydroxyapatite coatings *Appl. Surf. Sci.* **354** 373–9

[41] Bull S J 2005 Nanoindentation of coatings *J. Phys. D: Appl. Phys.* **38** 393–413

[42] Kokubo T and Takadama H 2006 How useful is SBF in predicting *in vivo* bone bioactivity? *Biomaterials* **27** 2907–15

[43] Gadelmawla E S, Koura M M, Maksoud T M A, Elewa I M and Soliman H H 2002 Roughness parameters *J. Mater. Process. Technol.* **123** 133–45

[44] Evgeny B, Hughes T, Eskin D, Evgeny B and T Hughes D E 2016 Effect of surface roughness on corrosion behaviour of low carbon steel in inhibited 4 M hydrochloric acid under laminar and turbulent flow conditions *Corros. Sci.* **103** 196–205

[45] Rho J Y, Ashman R B and Turner C H 1993 Young's modulus of trabecular and cortical bone material: Ultrasonic and microtensile measurements *J. Biomech.* **26** 111–9

[46] Ballarre J, Seltzer R, Mendoza E, Orellano J C, Mai Y W, García C and Ceré S M 2011 Morphologic and nanomechanical characterization of bone tissue growth around bioactive sol-gel coatings containing wollastonite particles applied on stainless steel implants *Mater. Sci. Eng.* C **31** 545–52

[47] Leyland A and Matthews A 2000 On the significance of the H/E ratio in wear control: a nanocomposite coating approach to optimised tribological behavior *Wear* **246** 1–11

[48] Charitidis C A, Skarmoutsou A, Tsetsekou A, Brasinika D and Tsiourvas D 2013 Nanomechanical properties of hydroxyapatite (HAP) with DAB dendrimers (poly-propylene imine) coatings onto titanium surfaces *Mater. Sci. Eng.* B **178** 391–9

[49] Hack H, Scully J and Dean S W J 2005 Electrochemical tests *Corrosion Tests and Standards: Application and Interpretation* ed R Baboian (ASTM International USA) ch 7 pp 107–30

[50] Radin S R and Ducheyne P 1993 The effect of calcium phosphate ceramic composition and structure on *in vitro* behavior: II. Precipitation *J. Biomed. Mater. Res.* **27** 35–45

[51] Wagener V, Schilling A, Mainka A, Hennig D, Gerum R, Kelch M, Keim S, Fabry B and Virtanen S 2016 Cell adhesion on surface-functionalized magnesium *ACS Appl. Mater. Interfaces* **8** 11998–2006

[52] Leidi M, Dellera F, Mariotti M and Maier J A M 2011 High magnesium inhibits human osteoblast differentiation *in vitro Magnes. Res.* **24** 1–6

[53] Castiglioni S, Cazzaniga A, Albisetti W and Maier J A M 2013 Magnesium and osteoporosis: Current state of knowledge and future research directions *Nutrients* **5** 3022–33